Research Square

Preprints are preliminary reports that have not undergone peer review.
They should not be considered conclusive, used to inform clinical practice,
or referenced by the media as validated information.

A Single [U-13C6]Glucose Tracer Enables Simultaneous Quantification of Integrated Multi-Tissue Metabolic Fluxes In Vivo

Yongliang Wang

yongliang.wang@henu.edu.cn

Henan University

Wei Lou

Henan University

Guoan Wang

Henan University

Dongxin Gao

Henan University

Wenlei Wang

Henan University

Mingjie Guo

Henan University

Xin Song

Henan University

Xinyu Zhao

Henan University

Zuchao Du

Henan University

Article

Keywords:

Posted Date: November 5th, 2026

DOI: https://doi.org/10.21203/rs.3.rs-11055611/v1

License: This work is licensed under a Creative Commons Attribution 4.0 International License.
Read Full License

Additional Declarations: There is **NO** Competing Interest.

A Single [U-$^{13}C_6$]Glucose Tracer Enables Simultaneous Quantification of Integrated Multi-Tissue Metabolic Fluxes In Vivo

Wei Lou[1, 2, &], Guoan Wang[1, 2, &], Dongxin Gao[1, 2], Wenlei Wang[1, 2], Mingjie Guo[1, 2], Xin Song[1, 2], Xinyu Zhao[1, #], Zuchao Du[1, #], Yongliang Wang[1, #]

[1] Huaihe Hospital (The Zhongzhou Laboratory for Integrative Biology)/Department of Hepatopancreatobiliary Surgery, The First Affiliated Hospital of Henan University, School of Medicine, Henan University, Kaifeng, Henan, 475000, China

[2] Basic Medical College, Henan University, Kaifeng, Henan, 475000, China

[&] These authors contributed equally

[#] Correspondence: Xinyu Zhao (shuijingxinyu@henu.edu.cn), Zuchao Du (202101237@hrbmu.edu.cn) and Yongliang Wang (yongliang.wang@henu.edu.cn)

Abstract

Precise simultaneous quantification of carbon fluxes in liver and skeletal muscle remains challenging due to overlapping metabolic pathways and incomplete correction of isotopic dilution in conventional stable-isotope tracing. Here we establish an integrated in vivo [$^{13}C_6$]-glucose tracing framework to absolutely quantify core glycolytic, gluconeogenic, lipogenic, TCA cycle and anaplerotic fluxes in mouse liver and skeletal muscle under steady state. Low-dose tracer infusion avoids disrupting endogenous metabolism, and our refined network resolves competing carbon routes with rigorous isotopic dilution correction. Orthogonal 2-deoxyglucose tracing is incorporated to specifically enable accurate quantification of skeletal muscle glucose uptake and support the calculation of carbon metabolic fluxes within skeletal muscle. We applied this platform to characterize tissue-specific metabolic remodeling triggered by fasting, high-fat diet, metformin and Aldometanib. This method detects subtle flux changes undetectable by standard isotopologue analysis. Our unified multi-tissue flux toolkit provides a robust resource to dissect interorgan carbon metabolism and evaluate metabolism-targeting therapeutics.

Main

Liver and skeletal muscle are central metabolic organs that coordinately govern systemic glucose homeostasis, lipogenesis, and oxidative metabolism in response to nutritional fluctuations, including fasting and high-fat dietary stress [1-4]. Dysregulated carbon partitioning, impaired tricarboxylic acid (TCA) cycle flux, and aberrant gluconeogenic/lipogenic remodeling in these tissues are hallmark drivers of insulin resistance, type 2 diabetes, and metabolic syndrome [3,5]. Despite their fundamental importance, precise quantification of interconnected hepatic and muscular metabolic fluxes remains technically challenging, largely due to the complexity of intertwined glycolytic, anaplerotic, lipogenic, and oxidative pathways, as well as dynamic substrate cycling between cytosolic and mitochondrial compartments [6-8].

Stable isotope tracing represents the gold-standard approach for quantifying in vivo metabolic flux, enabling high-resolution dissection of carbon routing through discrete metabolic nodes [7]. Conventional [^{13}C]glucose tracing strategies can only assess bulk TCA cycle turnover and gross pathway activity, yet fail to deconvolve biochemically overlapping carbon fluxes that define metabolic homeostasis [9]. These unresolved processes include PDH- and PC/ME-mediated TCA anaplerosis, substrate-specific glucose futile cycling, compartment-restricted de novo lipogenesis (DNL), fatty acid β-oxidation, and glutamine-fueled anaplerosis. Critically, current analytical frameworks lack unified mathematical models for simultaneous flux quantification in liver and skeletal muscle, the two dominant tissues controlling systemic glucose and lipid metabolism [10,11]. Furthermore, most existing pipelines do not incorporate rigorous corrections for isotopic dilution arising from glycogenolysis, basal TCA substrate recycling, and heterogeneous gluconeogenic precursors [12]. Collectively, these technical shortcomings limit the capacity to precisely quantify tissue-specific metabolic rewiring driven by nutritional stress or pharmacological modulation.

To address these methodological bottlenecks, here we establish a comprehensive, mathematically defined in vivo [$^{13}C_6$]glucose tracing flux analysis platform for simultaneous, absolute quantification of core glycolytic, gluconeogenic, lipogenic, TCA cycle, and anaplerotic/cataplerotic fluxes in mouse liver and skeletal muscle under metabolic steady state. Our refined tracer infusion paradigm employs low-dose [$^{13}C_6$]glucose delivery to preserve physiological metabolic homeostasis, avoiding

perturbation of endogenous glucose and lipid turnover [13]. By systematically simplifying redundant long-range isotopic pathways based on empirical isotopologue enrichment patterns, we construct a streamlined yet rigorous metabolic network model that resolves layered carbon fluxes, including tissue-specific glucose futile cycling, compartmentalized DNL precursor fluxes, reversible fumarate hydratase cycling, and glutamine- and methylmalonyl-CoA-dependent TCA anaplerosis.

A key advantage of this platform is its capacity to deconvolve parallel and competing carbon pathways: it distinguishes PDH- versus PC/ME-derived TCA cycle carbon input, separates lipogenic and oxidative pyruvate shuttling, and corrects isotopic dilution from glycogenolysis and endogenous substrate recycling in both liver and skeletal muscle. Combined with orthogonal 2-deoxyglucose (2-DG) glucose uptake tracing and selective metabolite infusion validation, our model enables robust calculation of absolute flux values for nearly all core nodes governing glucose and lipid homeostasis across nutritional and pharmacological conditions.

In summary, this study establishes an integrated, high-resolution in vivo metabolic flux quantification framework that unifies hepatic and skeletal muscle carbon network analysis. This technically rigorous and broadly adaptable method fills a critical gap in current metabolic tracing toolkits, provides a quantitative foundation for dissecting tissue-specific glucose and lipid metabolism, and enables precise mechanistic evaluation of metabolism-targeting therapeutic agents.

Methods

Animal models

All animal studies were conducted in accordance with the approved guidelines of the Ethics Committee of Henan University (Kaifeng, Henan Province, P. R. China). Twelve-week-old C57BL/6J male mice were purchased from Beijing HFK Bioscience Co., Ltd. (Beijing, P. R. China). Upon arrival, the mice were housed under a 12-h light/dark cycle at a controlled temperature of 23 ± 2°C with free access to water and a regular chow diet (1025, Beijing HFK Bioscience Co., Ltd.) or high fat diet (h10060, Beijing HFK Bioscience Co., Ltd.).

Mouse basal infusions

Mouse basal infusion studies were conducted with minor modifications based on the method described previously [14]. Briefly, Instech catheters (Part Number: BTPU-027) were implanted into the jugular vein 7 days prior to the experiments. Only mice that had regained more than 95% of their preoperative body weight were included in the study. Mice were fasted starting at 18:00 on the evening before the infusion study. All infusion studies commenced at 08:00 the following morning: awake mice, under gentle tail restraint, received a primed-continuous infusion of [$^{13}C_6$]glucose, 1,2,3,4,5,6-^{13}C-palmitate or [$^{13}C_3$]alanine (Cambridge Isotope Laboratories) at a rate of 39.3 μmol/min, 25.1 pmol/min or 200 pmol/min, respectively for 120 min.

For cohorts receiving [$^{13}C_6$]glucose infusion, a bolus injection of 2-deoxyglucose (2DG, 1 mg per mouse) was administered through the jugular venous catheter at the 85th minute of infusion. Blood samples were collected via tail vein puncture at 90 min and 120 min post initiation of infusion.

After the clamping procedure, the mice were anesthetized via intravenous injection of sodium pentobarbital through the pre-implanted jugular venous catheter, and blood samples, as well as specimens of liver and skeletal muscle (gastrocnemius and soleus) were rapidly harvested and snap-frozen with clamps precooled in liquid N_2. Then, tissues were stored at -80°C for subsequent analysis.

Design

Hepatic metabolic flux calculations

The [$^{13}C_6$]glucose-base flux calculations rely extensively on atom percent excess calculations for precursor and product metabolites, measured by LC/MS. To avoid disrupting the glucose and lipid metabolism in the physiological state of the animal model, We infused [$^{13}C_6$]glucose into mice via the jugular vein at ~10% of their glucose turnover (i.e., less than 9 μmol/(kg·min)) (Figure 1a). The glucose flux labeling pattern arises when [$^{13}C_6$]glucose is converted to [$^{13}C_3$]pyruvate via glycolysis in the liver. Subsequently, ^{13}C labeling is detectable in other TCA cycle intermediates as well as regenerated glucose (Figure 1b). The calculation of glucose flux was based on the dilution of the ^{13}C label and fractional contributions across TCA cycle and gluconeogenesis.

We found that the percentage of serum [$^{13}C_4$]glucose was lower than that of [$^{13}C_5$]glucose

in mice under both *ad libitum* regular chow diet (RC, 0.12% vs. 0.19%) and high-fat diet (HFD, 0.13% vs. 0.22%) feeding conditions, as well as in both RC-fed (0.24% vs. 0.45%) and HFD-fed (0.22% vs. 0.32%) overnight-fasted mice (Figure 1c). Thus, the contribution of the common metabolic pathway (denoted as i, Figure 1b) for generating serum [$^{13}C_4$]glucose and [$^{13}C_5$]glucose are negligible. Similarly, the percentage of serum [$^{13}C_4$]glucose was substantially lower than that of [$^{13}C_3$]glucose in mice under both *ad libitum* regular chow diet (RC, 0.12% vs. 0.86%) and high-fat diet (HFD, 0.13% vs. 1.03%) feeding conditions, as well as in both RC-fed (0.24% vs. 1.74%) and HFD-fed (0.22% vs. 1.72%) overnight-fasted mice (Figure 1c). Thus, the contribution of the common metabolic pathway (denoted as ii, Figure 1A) for generating serum [$^{13}C_4$]glucose and [$^{13}C_5$]glucose is negligible. In line with this, the common metabolic pathway (denoted as iii) for generating serum [$^{13}C_2$]glucose and [$^{13}C_3$]glucose is a component of pathway ii, thus its contribution is negligible. Of note, the metabolic pathways responsible for generating glucose via pathways i, ii, and iii are longer than the others, with their enrichments expected to be significantly lower. Collectively, the metabolic pathway responsible for generating [$^{13}C_1$]-, [$^{13}C_2$]-, [$^{13}C_3$]-, [$^{13}C_4$]-, [$^{13}C_5$]- and [$^{13}C_6$]glucose can be simplified as shown in Figure 1d.

The schematic diagram shown in Figure 1e and 1f illustrates the integrated hepatic glucose and lipid metabolic networks, where key metabolites (glucose, pyruvate, acetyl-CoA, and TCA cycle intermediates including citrate, oxaloacetate, malate, fumarate) form interconnected nodes. Glucose dynamically interconverts with glycogen via glycogenolysis ($V_{glycogenolysis}$) and glycogenesis ($V_{glycogenesis}$), while also feeding into pyruvate production. Pyruvate, in turn, serves as a central hub: it is generated not only from glucose but also via gluconeogenesis (V_{GNG}) fueled by amino acids/lactate and glycerol input. Notably, glucose engages in a futile cycle ($V_{glucose\ futile}$), which comprises two distinct metabolic loops. The first loop proceeds as: glucose is converted to pyruvate through glycolysis, and the resulting pyruvate is then transformed into oxaloacetate, which ultimately undergoes gluconeogenesis to regenerate glucose; this segment is composed of fluxes through pyruvate carboxylase (V_{PC}) and malic enzyme (V_{ME}). The second loop involves a more complex route: pyruvate derived from glucose is converted to citrate via either pyruvate dehydrogenase ($V_{PDH(T)}$) or pyruvate carboxylase ($V_{PC(T)}$);

this citrate then traverses the TCA cycle to generate oxaloacetate, which finally enters gluconeogenesis to form glucose again. Both loops contribute to $V_{glucose\ futile}$, representing a net flux where glucose is cycled through these pathways without net accumulation of end products, yet playing a role in metabolic regulation and substrate sensing [15].

Pyruvate further links to acetyl-CoA, a pivotal metabolite in lipid metabolism. Within the cytosol, pyruvate-derived acetyl-CoA (moved from mitochondria via citrate-malate shuttle, with citrate export tied to pyruvate dehydrogenase flux ($V_{PDH(DNL)}$), malic enzyme flux ($V_{ME(DNL)}$) and pyruvate caboxylase flux ($V_{PC(DNL)}$) drives *de novo* lipogenesis (V_{DNL}). Here, acetyl-CoA carboxylase (activity reflected in flux terms integrating cytosolic acetyl-CoA availability) converts acetyl-CoA to malonyl-CoA, initiating fatty acid chain elongation (V_{DNL}). Pyruvate generates acetyl-CoA and OAA through PDH and PC/ME, which then form citric acid under the action of CS (V_{CS}), and subsequently generate α-ketoglutaric acid under the action of isocitrate dehydrogenase (V_{IDH}). Afterwards, α-ketoglutaric acid generates succinic acid through OGDH (V_{OGDH}). Fatty acids (FA) enter the pathway through uptake ($V_{FA\ uptake}$), are converted to FA-CoA, and then generate acetyl-CoA via β-oxidation (V_{β}). Mitochondrial fluxes, such as those mediated by pyruvate dehydrogenase (V_{PDH}), pyruvate carboxylase (V_{PC}), and malic enzyme (V_{ME}), act as shuttles for intermediates between these organelles and the cytosol. The TCA cycle, supported by anaplerotic and cataplerotic shuttles like the malate-citrate shuttle (with $V_{FH(forward)}$ and $V_{FH(reverse)}$ governing fumarate-malate flux), drives both energy production and metabolite exchanges. Additionally, the TCA cycle receives anaplerotic inputs from two key pathways: glutamine is converted to α-ketoglutarate via glutaminase (V_{GLS}), directly feeding into the cycle; and methylmalonyl-CoA is transformed into succinate by methylmalonyl-CoA mutase (V_{MUT}), providing another critical anaplerotic input to TCA cycle intermediates. Given these interconnected metabolic relationships, flux balance analysis allows derivation of pathway flux equations.

As we have reported previously [16], glucose turnover is calculated by Eq. (1):

$$V_{glucose\ turnover} = \left(\frac{infusate\ [m+6] glucose\ inrichment}{serum\ [m+6] glucose\ inrichment} - 1 \right) * glucose\ infusion\ rate \quad (1)$$

In the state of metabolic equilibrium, as shown in Figure 1f, systemic glucose turnover equals the sum of fluxes across amino acid/lactate (V_{GNG}, this part of the flux includes the flux of glucose absorbed from the digestive tract), glycogenolysis ($V_{glycogenolysis}$), glycerol-mediated gluconeogenesis ($V_{glycerol}$), hepatic *de novo* lipogenesis (V_{DNL}), yield Eq. (2):

$$V_{glucose\ turnover} = V_{GNG} + V_{glycogenolysis} + V_{glycerol} + V_{DNL}$$

Glucose futile cycling rate equals the sum of the regeneration rates of [$^{13}C_1$]-, [$^{13}C_2$]-, [$^{13}C_3$]-, [$^{13}C_4$]-, [$^{13}C_5$]- and [$^{13}C_6$]glucose, calculated by Eq. (3):

$$V_{futile\ cycle} = \frac{S^{glucose\ futile}[sum]}{S^{G}[sum]} * V_{glucose\ turnover} \quad (3)$$

Where S^{G}[sum] represents the total enrichment of serum ^{13}C labelled glucose, yields Eq. (4):

$$S^{G}[sum] = S^{G}[m+6] + S^{G}[m+5] + S^{G}[m+4] + S^{G}[m+3] + S^{G}[m+2] + S^{G}[m+1] \quad (4)$$

$S^{futile\ cycle}$[sum] represents the total enrichment of serum ^{13}C labelled glucose derived from glucose futile flux. It should be noted that the [$^{13}C_6$]glucose in the futilely cycled glucose is derived from two [$^{13}C_3$]OAA molecules; therefore, its percentage equals the square of the percentage of [$^{13}C_3$]glucose, yields Eq. (5):

$$\begin{aligned} &S^{futile\ cycle}[sum] \\ &\quad = S^{G}[m+3]^2 + S^{G}[m+5] + S^{G}[m+4] + S^{G}[m+3] \\ &\quad + S^{G}[m+2] + S^{G}[m+1] \end{aligned} \quad (5)$$

As shown in Figure 1C, glucose derived from TCA cycle-generated oxaloacetate (OAA) consists of [$^{13}C_1$]glucose and a portion of [$^{13}C_2$]glucose. Their enrichments are expected to be equal, as both are produced via the same pathway; collectively, this yields Eq. (6):

$$V_{TCA} = V_{PC(T)} + V_{PDH(T)} + V_{ME(T)} = \frac{2S^{G}[m+1]}{S^{futile\ cycle}[sum]} * V_{glucose\ futile} \quad (6)$$

In contrast, the glucose generated via the PC and ME pathways equals the total futile cycling flux minus the flux of glucose generated via the TCA cycle, yields Eq. (7):

$$V_{PC} + V_{ME} = \frac{S^{futile\ cycle}[sum] - 2S^{G}[m+1]}{S^{futile\ cycle}[sum]} * V_{glucose\ futile} \quad (7)$$

Glucose in liver tissue is categorized into two types based on its source: one type is glucose absorbed from the blood, which will be further used for lipid synthesis (V_{TG}, composited of three carbon glycerol backbone ($V_{glycerol}$) and *de novo* lipogenesis, with a theoretical ratio of 1:3 between the two), glycogen synthesis (whose rate is equal to that of glycogenolysis), and futile cycling; the other type is generated through gluconeogenesis, including glucose converted from gluconeogenic amino acids/lactate, glycerol, and fatty acids via different metabolic pathways, as well as glucose produced by glycogenolysis. Thus, the fraction of between the former and latter can be measured as Eq. (8) and Eq. (9):

$$V_{TG} = V_{glycerol} + \frac{1}{3}(V_{PC(DNL)} + V_{ME(T)} + V_{ME(DNL)}) \quad (8)$$

$$\frac{V_{futile\ cycle} + V_{TG} - V_{glycogenesis}}{V_{glucose\ turnover}} = \frac{L^{G}[m+6]}{S^{G}[m+6] - S^{G}[m+3]^{2}} \quad (9)$$

The hepatic [$^{13}C_3$]citrate pool originates from the TCA cycle and DNL via PC and ME. However, this pool is diluted by citrate derived from acetyl-CoA—formed through PDH (Figure 1D). Based on the dilution ratio of [$^{13}C_3$]citrate, the following equation can be derived:

$$\frac{(V_{PC(T)} + V_{PC(DNL)} + V_{ME(T)} + V_{ME(DNL)}) * L^{Pyr}[m+3]}{V_{PC(T)} + V_{PC(DNL)} + V_{PDH(T)} + V_{PDH(DNL)} + V_{ME(T)} + V_{ME(DNL)}} = L^{Cit}[m+3] \quad (10)$$

After the ^{13}C-labeled citrate in mitochondria is shuttled to the cytoplasm, it is cleaved to form acetyl-CoA, which then forms [16-$^{13}C_1$]PA through DNL (as shown in Figure 1e). These fatty acids are rapidly esterified into triglycerides in the liver, transported to adipose tissue via apolipoproteins, and subsequently hydrolyzed to release free fatty acids back into the bloodstream. It can thus be seen that total hepatic DNL (V_{DNL}) is equivalent to the fatty acid in the circulation (S^{PA} [m+1]). At steady state, the ratio of S^{PA} [m+1 to glucose turnover is equal to the ratio of the molar mass of [16-$^{13}C_1$]PPA to that of [$^{13}C_6$]glucose. Collectively, DNL derived from [3,4,5-$^{13}C_3$]-, [3,5-$^{13}C_2$]- and [5-$^{13}C_1$]-citrate is given by Eq. (11):

$$k_1 = V'_{PC(DNL)} + V'_{ME(DNL)} = \frac{S^{PA}[m+1]}{S^{G}[m+6]} * V_{glucose\ turnover} \quad (11)$$

Based on the metabolic features illustrated in Figure 1e, we calculated the fractions of DNL derived from [3,4,5-$^{13}C_3$]-, [3,5-$^{13}C_2$]- and [5-$^{13}C_1$]-citrate relative to total PC/ME-supported DNL. The formula for total PC/ME-contributed DNL is defined as:

$$V_{PC(DNL)} + V_{ME(DNL)}$$

$$= \frac{S^{G}[m+6] + S^{G}[m+5] + S^{G}[m+4] + \frac{1}{2}S^{G}[m+3] + \frac{1}{2}S^{G}[m+2] + \frac{1}{2}S^{G}[m+1]}{S^{G}[m+6] + S^{G}[m+5] + S^{G}[m+4] + \frac{1}{2}S^{G}[m+3] + \frac{1}{2}S^{G}[m+2]} * k_1$$

(12)

Likewise, using the information from Figure 1e, we calculated the flux ratio between PDH and the PC/ME pathway:

$$k_2 = \frac{V_{PDH}}{V_{PC} + V_{ME}} = \frac{\left(\frac{L^{cit}[m+1]}{L^{cit}[m+3]} - \frac{L^{pyr}[m+1]}{L^{pyr}[m+3]}\right) * \left(S^{G}[m+3]^2 + \frac{1}{2}S^{G}[m+5] + \frac{1}{2}S^{G}[m+3]\right)}{\frac{1}{2}S^{G}[m+5] + S^{G}[m+4] + \frac{1}{2}\left(S^{G}[m+2] - S^{G}[m+1]\right)}$$

(13)

Thus, total DNL is given by Eq. (14)

$$V_{DNL} = \left(V_{PC(DNL)} + V_{ME(DNL)}\right) * (k_2 + 1) \quad (14)$$

In the state of metabolic equilibrium, the rate at which the liver takes up fatty acids from the blood is equal to the rate of their oxidative decomposition, thus leading to the following formula：

$$V_{\beta} = V_{FA\ uptake} = V_{DNL} \quad (15)$$

As shown in Figure 1D, the flux through isocitrate dehydrogenase (IDH) is equal to V_{TCA}, and the flux through citrate synthase (CS) is equal to sum of V_{DNL} and V_{TCA}, yields Eq. (16) and (17):

$$V_{IDH} = V_{TCA} \quad (16)$$

$$V_{CS} = V_{DNL} + V_{TCA} \quad (17)$$

The glutamate pool is formed by two fluxes: a fraction of glutamate is generated by IDH-mediated conversion of isocitrate to αKG, which is rapidly exchanges with glutamate and reaches isotopic equilibrium; the remaining fraction is produced through the net reaction of glutaminase (GLS) ($V_{GLS(net)}$). As shown in Figure 1e and 1f, by measuring the [2-$^{13}C_1$]citrate, [3,4-$^{13}C_2$]citrate and [5-$^{13}C_1$]citrate derived [m+1]glutamate enrichment and dividing it by the detected hepatic [m+1]glutamate enrichment, we can determine the fraction of glutamate derived directly from the net flux of GLS. First, theoretical [3,4-$^{13}C_2$]citrate enrichment can be calculated using the following equation:

$$k_3 = \frac{L^{Cit}[m+3] * \frac{1}{2} S^G[m+1]}{S^G[m+3]^2 + \frac{1}{2} S^G[m+5] + \frac{1}{2} S^G[m+3]} \quad (18)$$

Based on the dilution ratio of [m+1]glutamate, we derived the following equation:

$$V_{Gls(net)} = k_4 * V_{IDH} \quad (19)$$

Where

$$k_4 = \frac{L^{Cit}[m+1] + k_3 - L^{Glu}[m+1]}{L^{Glu}[m+1]} \quad (20)$$

Similarly, the succinate pool is created by two fluxes: a fraction of glutamate is generated by Methylmalonyl-CoA mutase (MUT) ($V_{MUT(net)}$) and Succinyl-CoA synthetase (SCS) ($V_{SCS(net)}$). Collectively, the fractional contribution of α-ketoglutarate dehydrogenase (OGDH) (V_{OGDH}) and $V_{MUT(net)}$+ $V_{SCS(net)}$ can be calculated using Eq. (21) and (22):

$$V_{OGDH} = V_{IDH} + V_{GLS(net)} \quad (21)$$

$$\frac{V_{OGDH}}{V_{MUT(net)} + V_{SCS(net)}} = \frac{L^{succinate}[m+1]}{L^{Glu}[m+1] - L^{succinate}[m+1]} \quad (22)$$

Lastly, from the metabolic characteristics illustrated in Figures 1d and 1f, the reverse $V_{FH(R)}$ and forward $V_{FH(F)}$ fluxes of fumarate hydratase (FH) were determined using the following equations:

$$V_{FH(R)} = V_{glucose\ turnover} * \frac{S^G[m+2] - S^G[m+1]}{S^G[sum]} \quad (23)$$

$$V_{FH(forward)} = V_{FH(reverse)} + V_{OGDH} + V_{MUT(net)} + V_{SCS(net)} \quad (24)$$

Using the above equations, we substitute the absolute rate of glucose turnover and then solve for the absolute rates of hepatic $V_{futile\ cycle}$, V_{TCA}, $V_{PC}+V_{ME}$, V_{β} (equal to V_{DNL}), $V_{glycerol}$, V_{TG}, $V_{GNG}+V_{digestion}$, $V_{glycogenolysis}$, $V_{FA\ uptake}$, $V_{PC(DNL)}+V_{ME(DNL)}$, $V_{PC(T)}+V_{ME(T)}$, $V_{PDH(DNL)}$, $V_{PDH(T)}$, V_{CS}, V_{IDH}, $V_{GlS(net)}$, $V_{MUT(net)}+V_{SCS(net)}$, V_{OGDH}, $V_{FH(R)}$, and $V_{FH(F)}$.

Skeletal muscle metabolic flux calculations

The schematic diagram presented in Figure 1f depicts core glucose and oxidative metabolic networks in skeletal muscle, with central metabolites (glucose, pyruvate, acetyl-CoA, and TCA cycle intermediates including citrate, oxaloacetate, malate and fumarate) forming tightly connected metabolic nodes. Glucose undergoes bidirectional exchange with glycogen through $V_{glycogenesis}$ and $V_{glycogenolysis}$, and glucose-derived pyruvate constitutes a primary metabolic hub. In skeletal muscle, pyruvate can enter the mitochondria via multiple routes: pyruvate is oxidized through pyruvate dehydrogenase ($V_{PDH(T)}$) to produce acetyl-CoA, or converted to oxaloacetate by pyruvate carboxylase ($V_{PC(T)}$); malic enzyme ($V_{ME(T)}$) mediates the interconversion between malate and pyruvate to support cytosolic-mitochondrial metabolite exchange.

Pyruvate-derived acetyl-CoA converges with acetyl-CoA originating from fatty acid oxidation to fuel the TCA cycle. Circulating fatty acids (FA) are taken up ($V_{FA\ uptake}$) and converted to FA-CoA, which yields mitochondrial acetyl-CoA via β-oxidation (V_{β}). Mitochondrial acetyl-CoA condenses with oxaloacetate to form citrate, initiating the TCA cycle. Forward and reverse fumarate-hydratase fluxes ($V_{FH(F)}$) and ($V_{FH(R)}$) govern the reversible interconversion between malate and fumarate, supporting cataplerotic and anaplerotic exchange across the malate shuttle. Unlike the liver, skeletal muscle lacks robust gluconeogenic machinery and cytosolic de novo lipogenesis pathways; the PC/ME axis primarily functions to maintain TCA cycle anaplerosis and facilitate redox balance rather than supporting glucose production or lipogenesis. The coordinated fluxes of $V_{PDH(T)}$, $V_{PC(T)}$ and $V_{ME(T)}$ sustain carbon substrate supply to the TCA cycle, coordinating glucose and fatty acid catabolism to meet the energy demand of skeletal muscle. Based on this interconnected topological framework, stable isotope tracing enables quantification of individual pathway fluxes.

To calculate glucose uptake ($V_{glucose\ uptake}$) under metabolic steady state, a single bolus injection of 2-DG (1 mg per mouse) was administered via the jugular vein catheter. Blood samples were collected from the tail vein at 90 and 120 min post-injection (Figure 1a). Consistent with our previous report [17], $V_{glucose\ uptake}$ was quantified using Eq. (25):

$$V_{glucose\ uptake} = \frac{organ\ levels\ of\ \ 2\text{-}DG}{\Delta 2\text{-}DG} * V_{glucose\ turnover} \quad (25)$$

The [$^{13}C_6$]glucose pool in skeletal muscle is diluted by unlabeled glucose released via glycogenolysis ($V_{glycogenolysis}$), from which we derived the following equation:

$$\frac{V_{glucose\ uptake} - V_{glycogeneolysis}}{V_{glycogeneolysis}} = \frac{G^{Pyr}[m+3]}{S^G[m+6] - S^G[m+3]^2 + \frac{1}{2}S^G[m+5] + \frac{1}{2}S^G[m+3]} \quad (26)$$

As shown in Figure 2Sa, the total TCA flux (V_{TCA}), equivalent to V_{CS} or V_{IDH}, is defined as the sum of $V_{PDH(T)}$, $V_{PC(T)}$, $V_{ME(T)}$, and V_β, yields Eq. (27) and (28):

$$V_{TCA} = V_{CS} = V_{IDH} \quad (27)$$

$$V_{TCA} = V_{PC(T)} + V_{PDH(T)} + V_{ME(T)} + V_\beta = V_{glucose\ uptake} + V_\beta \quad (28)$$

In skeletal muscle, the [$^{13}C_3$]citrate pool arises from TCA cycle flux supported by PC and ME activity. This isotopic pool is nevertheless diluted by [$^{13}C_2$]citrate originating from acetyl-CoA generated via PDH. From the dilution ratio of [$^{13}C_3$]citrate, the equation below can be derived:

$$\frac{V_{PC(T)} + V_{ME(T)}}{V_{TCA}} = \frac{G^{Cit}[m+3]}{G^{Pyr}[m+3]} \quad (29)$$

$$\frac{(V_{PC(T)} + V_{ME(T)}) * G^{Pyr}[m+3]}{(V_{PC(T)} + V_{ME(T)}) * G^{Pyr}[m+2] + V_{PDH(T)} * k_3} = \frac{G^{Cit}[m+3]}{G^{Pyr}[m+3]} \quad (30)$$

Where

$$k_5 = G^{Pyr}[m+3] + G^{Pyr}[m+2] * \frac{\frac{1}{2}S^G[m+1]}{S^G[sum]} \quad (31)$$

Similar to the hepatic glutamate pool, the skeletal muscle glutamate pool is generated via IDH-catalyzed conversion of isocitrate to (V_{IDH}) and the net reaction of glutaminase (GLS)

($V_{GLS(net)}$). Accordingly, the theoretical [3,4-$^{13}C_2$]citrate enrichment can be calculated using the following equation:

$$k_6 = \frac{G^{Cit}[m+3] * \frac{1}{2} S^G[m+1]}{S^G[m+6] + \frac{1}{2} S^G[m+5] + \frac{1}{2} S^G[m+3]} \quad (32)$$

From the dilution ratio of skeletal muscle [m+1]glutamate, we derived the following equation:

$$\frac{(G^{Cit}[m+1] + k_6) \quad * V_{IDH}}{V_{IDH} + V_{Gls(net)}} = G^{Glu}[m+1] \quad (33)$$

$$V_{Gls(net)} = \frac{G^{Cit}[m+1] + k_6 - G^{Glu}[m+1]}{G^{Glu}[m+1]} * V_{IDH} \quad (34)$$

The succinate pool (V_{OGDH}) is sustained by IDH (V_{IDH}) and $V_{GLS(net)}$, can be calculated using Eq. (35):

$$V_{OGDH} = V_{IDH} + V_{GLS(net)} \quad (35)$$

Analogous to hepatic FH flux, the net FH flux of skeletal muscle is calculated as follows:

$$V_{FH(net)} = V_{OGDH} + V_{MUT(net)} + V_{SCS(net)} \quad (36)$$

Results

[$^{13}C_6$]glucose tracing reveals fasting remodels hepatic TCA cycle, gluconeogenic, and lipogenic flux homeostasis in chow- and high-fat-fed mice

To assess the alterations of glucose metabolism and TCA under different physiological condition, we infused mice with [$^{13}C_6$]glucose at a rate of 39.3 μg/min for 120 min (Figure 1a). Consistent with our previous studies [16,18], this approach theoretically generates high-mass isotopologues in TCA metabolites according to Figure 1b. In addition, at metabolic equilibrium, the percentage of the tracer in the blood is approximately 10% (Figure 1c), which is generally considered not to disrupt the physiological metabolism of mice [12,13]. Based on the distribution patterns of glucose labeled with distinct isotopic tracers and the principles outlined in the Design section, the hepatic metabolic pathway is simplified as illustrated in Figure 1d–f.

RF mice exhibited elevated isotopic labeling of pyruvate, glutamate, glutamine, succinate, fumarate m+1 and malate at distinct isotopologue positions, whereas citrate labeling remained unaltered (Figure 1Sa-g). To correct for systemic tracer recirculation, we further analyzed glucose-normalized relative enrichment. Total relative ^{13}C-labeled hepatic pyruvate enrichments were comparable between fasting RF mice and ad libitum-fed RC controls. While m+1 and m+2 pyruvate isotopologue enrichments were similar across groups, RF mice possessed significantly elevated m+3 pyruvate enrichment (Figure 2a). Conversely, total ^{13}C isotopic enrichment of multiple TCA cycle intermediates, including citrate, glutamate, glutamine, succinate, fumarate and malate, was significantly suppressed in RF mice. RF mice exhibited lower m+1 and m+2 enrichments for citrate, glutamate, glutamine and succinate, without altered m+3 citrate levels. For fumarate, only m+2 isotopologue enrichment was reduced in RF mice, with m+1 fumarate unchanged. In malate, RF mice displayed significant decreases in m+1 and m+2 enrichment, whereas m+3 malate isotopologue abundance was comparable between groups (Figure 2b-g). Thus, these divergent labeling profiles upon normalization indicate fasting reshapes hepatic carbon partitioning and reduces tracer incorporation into selected TCA intermediates in chow-fed mice.

To quantify the extent of these fasting-induced alterations in carbon incorporation, we carried out quantitative flux analysis. This analysis demonstrated that RF mice showed substantially decreased whole-body glucose turnover ($V_{glucose\ turnover}$). In line with the altered TCA isotopic labeling, RF mice exhibited markedly lower hepatic glucose futile cycle flux ($V_{futile\ cycle}$), combined pyruvate carboxylase and malic enzyme flux ($V_{PC}+V_{ME}$), glycogenolysis ($V_{glycogenolysis}$), and glycerol gluconeogenic flux ($V_{glycerol}$) relative to RC counterparts (Figure 2h). Combined pyruvate carboxylase/ malic enzyme and pyruvate dehydrogenase fluxes dedicated to lipogenesis ($V_{PC(DNL)}+V_{ME(DNL)}$ and $V_{PDH(DNL)}$, respectively), were also robustly diminished in RF animals (Figure 2i). In addition, hepatic fatty acid β-oxidation flux (V_{β}) was strongly reduced in RF mice (Figure 2j). Intriguingly, net gluconeogenic flux (V_{GNG}) diverged sharply between groups: RC mice showed negative net V_{GNG}, consistent with net glucose uptake by the liver, while RF mice displayed positive net hepatic gluconeogenesis (Figure 2k). Consistent with the suppressed hepatic TCA cycle intermediate labeling, nearly all core TCA cycle fluxes,

including overall TCA flux (V_{TCA}), pyruvate dehydrogenase flux (V_{PDH}), combined ($V_{PC(T)}$ +$V_{ME(T)}$), citrate synthase flux (V_{CS}), isocitrate dehydrogenase flux (V_{IDH}), net glutaminolysis flux ($V_{GLS(net)}$), oxoglutarate dehydrogenase flux (V_{OGDH}), reverse fumarate hydratase flux ($V_{FH(R)}$) and forward fumarate hydratase flux ($V_{FH(F)}$), were significantly lower in RF mice relative to RC controls. Moreover, net combined methylmalonyl-CoA mutase and succinyl-CoA synthetase flux ($V_{MUT(net)}$ +$V_{SCS(net)}$) exhibited distinct patterns between groups, with negative net flux observed in RC mice and positive net flux in RF mice (Figure 2l).

Similar to RF mice, overnight-fasted high-fat-fed (HF) mice exhibited elevated isotopic labeling of pyruvate, citrate, glutamate, glutamine, succinate, fumarate m+1 and malate at distinct isotopologue positions (Figure 1Sh-n). However, following normalization to account for tracer recirculation, total relative ^{13}C enrichment of hepatic pyruvate was comparable between HFD and HF groups. At the isotopologue level, pyruvate m+1, m+2 and m+3 enrichments exhibited no significant differences upon fasting in HFD mice (Figure 2m). By contrast, overnight fasting markedly suppressed total ^{13}C labeling of citrate, glutamate, glutamine, succinate and fumarate in HF mice. Specifically, HF mice displayed significantly reduced m+1 and m+2 citrate enrichment. Glutamate m+1 and m+2 isotopologue abundances were also lower in HF relative to HFD controls. Similarly, glutamine m+1 and m+2 labeling, total glutamine enrichment, succinate m+2 enrichment and total succinate enrichment were all diminished after fasting. For fumarate, both m+2 isotopologue enrichment and total ^{13}C-fumarate labeling were significantly decreased in HF mice. No consistent fasting-induced changes in malate isotopologue labeling (m+1, m+2, m+3) or total malate ^{13}C enrichment were detected between groups (Figure 2n–s).

Quantitative flux calculations revealed profound suppression of multiple glucose metabolic fluxes after overnight fasting in high-fat-fed mice. $V_{glucose\ turnover}$, $V_{futile\ cycle}$, combined V_{PC} + V_{ME}, $V_{glycogenolysis}$, and $V_{glycerol}$ were all significantly reduced in HF mice compared with *ad libitum* HFD controls (Figure 2t). These flux reductions align closely with the attenuated hepatic TCA cycle carbon labeling observed in HF animals, demonstrating that fasting globally restrains hepatic glucose substrate turnover and gluconeogenic precursor fluxes in the setting of high-fat feeding. Consistent with the global suppression of hepatic carbon metabolism, fluxes supporting DNL were also

markedly reduced after overnight fasting. Furthermore, lipogenic $V_{PC(DNL)}$+$V_{ME(DNL)}$ and $V_{PDH(DNL)}$ were significantly lower in HF mice relative to HFD controls (Figure 2u). These results indicate that fasting potently restricts carbon precursor supply for hepatic *de novo lipogenesis* in high-fat diet-fed animals, alongside the concurrent repression of gluconeogenic and TCA cycle fluxes. Hepatic V_{β} was substantially lower in overnight-fasted HF mice compared with fed HFD controls (Figure 2v). Notably, V_{GNG} exhibited a striking directional shift: HFD mice displayed robust net glucose uptake with negative V_{GNG}, whereas HF animals switched toward net hepatic glucose production, leading to a highly significant difference between groups (Figure 2w). Collectively, these data reveal that fasting in high-fat-fed animals suppresses hepatic fatty acid catabolism while rewiring net hepatic glucose balance toward gluconeogenesis, even amid broad reductions in carbon precursor fluxes supporting lipogenesis and substrate cycling. To further dissect the remodeling of hepatic mitochondrial metabolism, we quantified core tricarboxylic acid cycle and associated anaplerotic/cataplerotic fluxes. Overnight fasting significantly reduced overall V_{TCA}, V_{PDH}, V_{CS}, and V_{IDH} in HF mice compared with HFD controls. Consistent with depressed mitochondrial oxidation, V_{OGDH}, $V_{FH(R)}$, $V_{FH(F)}$, as well as $V_{GLS(net)}$ were all diminished upon fasting. By contrast, $V_{PC(T)}$ + $V_{ME(T)}$ and $V_{MUT(net)}$ + $V_{SCS(net)}$ did not differ significantly between groups (Figure 2x). These data demonstrate that fasting broadly suppresses forward TCA cycle flux and mitochondrial oxidative metabolism in livers of high-fat-fed mice, largely through limiting pyruvate entry and glutamine-supported anaplerosis, while preserving basal pyruvate cycling capacity.

To verify the fasting-induced changes in V_{GNG} and V_{β}, we conducted infusion of $^{13}C_3$-alanine and 1,2,3,4,5,6-^{13}C-palmitate via jugular vein catheterization. These tracer studies revealed that fasting elevated whole-body alanine turnover and promoted alanine tracer incorporation into gluconeogenesis (Figure 1So). Unexpectedly, we observed marked increases in palmitate tracer incorporation into TCA cycle intermediates upon fasting. Together, these data demonstrate that fasting enhances amino acid-fueled gluconeogenesis (Figure 1Sp). Despite reduced overall hepatic V_{β}, fasting stimulates the activity of fatty acid β-oxidation (Figure 1Sq).

To evaluate fasting-mediated changes in carbohydrate and lipid metabolism in skeletal

muscle (Figure 2Sa), tracer studies revealed that modest perturbations in select isotopologue fractions of muscle pyruvate, citrate, glutamate, glutamine, succinate, fumarate and malate upon fasting (Figure 2Sb-h). Nevertheless, tracer recirculation-corrected data demonstrated that fasting markedly diminished ^{13}C enrichment in these metabolites (Figure 3a-g). Quantitative flux calculations showed that fasting suppressed skeletal muscle $V_{glucose\ uptake}$, $V_{glycogenolysis}$, $V_{PC(T)} + V_{ME(T)}$, $V_{PDH(T)}$, V_{CS}, V_{IDH}. By contrast, global V_{TCA}, V_{β}, $V_{GLS(net)}$, V_{OGDH}, combined $V_{MUT(net)} + V_{SCS(net)}$, and net V_{FH} flux remained unaltered (Figure 3h). Very similarly, while fasting did not alter raw ^{13}C enrichment of muscle pyruvate, citrate, glutamate, glutamine, succinate, fumarate and malate (Figure 2Si-o), it markedly lowered relative tracer incorporation into these intermediates (Figure 3I-o). Meanwhile, fasting significantly reduced $V_{glucose\ uptake}$, $V_{glycogenolysis}$, $V_{PC(T)} + V_{ME(T)}$, $V_{PDH(T)}$, V_{CS}, V_{IDH}, V_{OGDH}, and net V_{FH} flux. Fasting increased negative $V_{MUT(net)} + V_{SCS(net)}$, whereas V_{TCA}, V_{β} and $V_{GLS(net)}$ remained unchanged (Figure 3p).

[$^{13}C_6$]glucose analysis reveals Aldometanib-induced hepatic metabolic remodeling and inhibited skeletal muscle glucose carbon flux

To further explore the mechanism by which Aldometanib (Ald), a candidate agent with proven efficacy in ameliorating diet-induced glucose dyshomeostasis, improves insulin sensitivity, we performed ^{13}C-glucose infusions in Ald-treated HFD-fed mice. Consistent with improved metabolic phenotype, Ald administration significantly decreased relative fat mass, accompanied by a robust increase in lean mass fraction (Figure 3Sa). Raw hepatic ^{13}C enrichment analysis revealed that Aldometanib altered isotopic labeling in only a limited set of hepatic glycolytic and TCA cycle intermediates. Ald increased total ^{13}C enrichment of pyruvate, citrate and glutamate: it suppressed pyruvate m+1, elevated pyruvate m+2/m+3 and citrate m+1, and enhanced glutamate m+1 labeling. Succinate showed a trend of increased ^{13}C enrichment (p=0.065). All other assessed isotopic parameters for citrate, glutamine, fumarate and malate were unchanged (Figure 3Sb-h). Next, we normalized these raw enrichment values to correct for systemic tracer recirculation and quantify relative tracer incorporation in the liver. Relative isotopic labeling analysis recapitulated core changes observed in raw enrichment profiles. Ald significantly enhanced relative total ^{13}C enrichment of pyruvate, citrate and glutamate. While relative pyruvate m+1 was unchanged, pyruvate m+2 and m+3 fractions increased

significantly. Ald induced coordinated elevation of citrate m+1 and m+2, together with higher glutamate m+1 and m+2 labeling. In addition, relative succinate m+1, m+2 and total succinate enrichment were markedly increased. No significant differences in relative ^{13}C labeling were found for glutamine, fumarate or malate (Figure 4a-g). Based on the resolved isotopologue distributions, we next performed metabolic flux analysis to quantitatively assess hepatic carbon fluxes. Calculated flux values revealed that Ald administration significantly increased whole-body glucose turnover. At the hepatic level, Ald robustly elevated $V_{futile\ cycle}$, the combined $V_{PC} + V_{ME}$, $V_{glycogenolysis}$, and $V_{glycerol}$ (Figure 4h). Further analysis of fluxes supporting de novo lipogenesis (DNL) demonstrated that Ald markedly increased $V_{PC(DNL)}+V_{ME(DNL)}$ and $V_{PDH(DNL)}$ (Figure 4i). In addition, Ald treatment induced a substantial rise in V_{β} (Figure 4j), alongside a pronounced reduction in net gluconeogenic flux V_{GNG} (Figure 4k). We further examined TCA cycle and associated anaplerotic/cataplerotic fluxes. Ald significantly increased $V_{PDH(T)}$, V_{CS} and $V_{FH(R)}$, while V_{TCA}, $V_{PC(T)} + V_{ME(T)}$, V_{IDH}, $V_{GLS(net)}$, $V_{MUT(net)} + V_{SCS(net)}$, V_{OGDH} remained unaltered. $V_{FH(F)}$ showed a trend toward elevation with a *p*-value of 0.059 (Figure 4l).

We performed ^{13}C stable isotope tracing to evaluate skeletal muscle carbon metabolism. Raw and normalized isotopic enrichment of pyruvate and TCA-cycle intermediates (citrate, glutamate, glutamine, succinate, fumarate, malate; m+1/m+2/m+3 isotopologues) were comparable between HF and Ald groups. Thus, Ald exerts prominent effects on hepatic carbon flux without majorly altering skeletal muscle TCA carbon trafficking (Figure 3Si-n and Figure 4m-s).

We characterized skeletal muscle carbon metabolism via stable ^{13}C tracing and measured both raw and normalized isotopic enrichment of pyruvate and TCA-cycle intermediates across m+1, m+2, and m+3 isotopologues. No significant intergroup differences in labeling patterns were detected for citrate, glutamate, glutamine, succinate, fumarate, and malate. Quantitative flux calculations further defined skeletal muscle carbon flow: Ald significantly suppressed $V_{glucose\ uptake}$, $V_{glycogenolysis}$, $V_{PDH(T)}$, V_{CS}, V_{IDH}. V_{TCA} (p=0.065) and V_{OGDH} (p=0.076) showed borderline non-significant reductions, while $V_{PC(T)} + V_{ME(T)}$, V_{β}, $V_{GLS(net)}$, $V_{MUT(net)} + V_{SCS(net)}$, and net V_{FH} were comparable between groups (Figure 4t). Together, these data indicate that Ald restrains glucose carbon flux into skeletal muscle TCA cycle, an effect unaccompanied by detectable shifts in metabolite

isotopic enrichment. Although Ald reduces glucose uptake under fasting conditions and restricts glucose carbon flux into the skeletal muscle TCA cycle, this treatment exerts beneficial effects on mitochondrial function.

[$^{13}C_6$]glucose tracing reveals metformin-mediated rewiring of hepatic metabolism and enhanced skeletal muscle anaplerotic flux

We further assessed the effects of metformin, a first-line clinically used drug, on glucose and lipid metabolism. Body composition analysis revealed that, metformin treatment did not alter the relative percentage of fat mass or lean mass when compared with vehicle-treated HFD animals. We next performed hepatic ^{13}C stable isotope tracing to measure raw isotopic enrichment of glycolytic and TCA-cycle intermediates. Metformin significantly decreased pyruvate m+1 enrichment while increasing pyruvate m+2, m+3 and overall total ^{13}C-pyruvate labeling. Within TCA metabolites, metformin elevated total ^{13}C-fumarate enrichment and fumarate m+1, together with a borderline increase in fumarate m+2 (p=0.052). No consistent differences were observed for citrate, glutamate, glutamine, succinate and malate isotopologues, though total ^{13}C-malate enrichment exhibited a non-significant downward trend in metformin-treated animals (p=0.07) (Figure 4Sa-h). Normalized isotopic enrichment analysis yielded highly congruent findings. Metformin reduced normalized ^{13}C-pyruvate m+1 and markedly enhanced normalized pyruvate m+2, m+3 and total pyruvate labeling. In the TCA cycle, normalized fumarate m+1, m+2 and cumulative fumarate enrichment were significantly elevated upon metformin administration. Isotopic enrichment of citrate, glutamate, glutamine, succinate and malate remained unaltered after normalization (Figure 5a-g).

Quantitative flux calculations demonstrated enhanced hepatic carbon turnover following metformin intervention. Metformin significantly increased $V_{glucose\ turnover}$, and the combined flux V_{PC} + V_{ME}. No significant alterations were detected in $V_{futile\ cycle}$ and $V_{glycogenolysis}$. Meanwhile, $V_{glycerol}$ showed a marginal increase in metformin-treated animals (p=0.056) (Figure 5h). Further quantification of lipogenic precursor fluxes revealed a non-significant rise in $V_{PC(DNL)}$+$V_{ME(DNL)}$, while $V_{PDH(DNL)}$ was significantly upregulated after metformin administration (Figure 5i). V_{β} showed a marginal elevation in the metformin group (p=0.056) (Figure 5j), whereas no obvious change was observed in net hepatic gluconeogenesis flux V_{GNG} between the two groups (Figure 5k). Analysis of tricarboxylic

acid (TCA) cycle fluxes showed that total $V_{PC(T)}$ + $V_{ME(T)}$, was markedly reduced upon metformin treatment. No significant differences were observed for V_{TCA}, $V_{PC(T)}$ + $V_{ME(T)}$, V_{CS}, V_{IDH}, $V_{GLS(net)}$, $V_{MUT(net)}$ + $V_{SCS(net)}$, V_{OGDH}, $V_{FH(R)}$ and $V_{FH(F)}$ (Figure 5l).

Skeletal muscle ^{13}C isotopic enrichment was characterized upon metformin treatment. The enrichment of malate m+1 isotopologue was significantly elevated in the metformin group (Figure 4Si-o). After normalization to relative enrichment, the overall labeling patterns of pyruvate, citrate, glutamate, glutamine, succinate, fumarate and malate isotopologues were largely comparable between groups, with no additional consistent alterations detected for other measured intermediates (Figure 5m-s). Then, Skeletal muscle metabolic fluxes were quantified using ^{13}C tracing. Metformin significantly increased $V_{PC(T)}$ + $V_{ME(T)}$, total TCA flux V_{TCA}, β-oxidation flux V_{β}, and net glutaminolysis $V_{GLS(net)}$. No significant shifts were detected for $V_{glucose\ uptake}$, $V_{glycolysis}$, $V_{PDH(T)}$, V_{CS}, V_{IDH}, V_{OGDH}, $V_{MUT(net)}$ + $V_{SCS(net)}$, and $V_{FH(net)}$ following metformin exposure (Figure 5h).

Discussion

Here, we establish an integrated in vivo tracing framework to simultaneously quantify absolute carbon fluxes in mouse liver and skeletal muscle under metabolic steady state. Conventional stable-isotope approaches are often restricted to single-tissue analysis and struggle to disentangle overlapping anaplerotic, lipogenic and glycolytic pathways [19-21]. Furthermore, incomplete correction for isotopic dilution originating from glycogenolysis and substrate recycling introduces systematic bias into flux estimations [22,23]. Our refined metabolic network model addresses these limitations by resolving competing carbon routing, while orthogonal 2-deoxyglucose tracing is incorporated to quantify skeletal muscle glucose uptake and enable robust calculation of intramuscular carbon metabolic fluxes. Methodological validation via independent metabolite infusion experiments supports the reliability of absolute flux outputs across distinct nutritional and pharmacological contexts. Recent advances in computational modeling, including tissue-specific genome-scale metabolic models and machine-learning-based digital twin frameworks, further underscore the power of integrating multi-omics data with flux analysis to capture tissue-specific metabolic heterogeneity [24,25].

We applied this multi-tissue quantification platform to characterize metabolic remodeling

triggered by fasting and high-fat diet feeding. Notably, we resolve a key contradiction: while fasting reduces absolute rates of hepatic fatty acid β-oxidation and amino acid/lactate-mediated gluconeogenesis, supplementary tracing with 1,2,3,4,5,6-^{13}C-palmitate and [$^{13}C_3$]alanine confirms fasting enhances the relative activity of these pathways—uncovering an “activity-flux dissociation” driven by metabolic resource prioritization [26,27]. This observation parallels findings from lipid metabolic flux analysis (Lipid-MFA), which demonstrated that flux through fatty acid synthase and very long-chain fatty acid elongation pathways can decrease while relative pathway activities remain elevated under certain metabolic stress conditions [28]. Under nutrient deprivation, systemic substrate availability declines. The liver upregulates intrinsic pathway capacity to maximize efficient utilization of available carbon sources, yet limited substrate supply constrains maximal absolute throughput. This decoupling carries substantial conceptual implications: measurements relying only on isotopologue enrichment or pathway enzyme activity cannot reliably reflect net metabolic flux [7]. It emphasizes that distinguishing relative pathway activity from absolute carbon turnover is indispensable for interpreting adaptive metabolic responses.

Beyond nutritional challenges, our flux profiling reveals divergent tissue-specific metabolic signatures in response to metformin and Aldometanib. Consistent with prior mechanistic reports, metformin predominantly remodels hepatic anaplerotic and gluconeogenic fluxes [29,30]. In contrast, Aldometanib exerts coordinated effects on both liver and skeletal muscle, reshaping inter-organ carbon partitioning to improve systemic insulin sensitivity [31,32]. Notably, studies modeling high-sugar diet-induced metabolic dysregulation in Drosophila muscle have identified distributed control of glycolytic flux and altered NAD(H)-dependent reactions, highlighting the importance of tissue-specific metabolic models for understanding drug and dietary interventions [24]. These divergent flux fingerprints illustrate why multi-tissue simultaneous quantification is critical for dissecting drug action; single-organ measurements risk oversimplifying systemic metabolic regulation and may mask tissue-selective pharmacological effects [33].

Several technical considerations warrant discussion. The current model is built upon steady-state tracer infusion in conscious mice, which preserves physiological metabolism yet restricts direct extension to acute, rapidly transitioning metabolic states. In addition,

our framework focuses on core carbon pathways centered on glucose-derived carbon. Future iterations may integrate long-chain fatty acid and amino acid multi-tracer designs to achieve a more complete view of interconnected carbon, nitrogen and lipid metabolism [6]. Although we have implemented corrections for major sources of isotopic dilution, compartmental substrate exchange between cytosol and mitochondria remains difficult to fully deconvolve using whole-tissue extracts alone. Combining this flux modeling strategy with subcellular fractionation, genetically encoded metabolic sensors and spatial flux mapping approaches represents a promising direction to further refine spatial resolution, enabling precise dissection of metabolic alterations across functionally distinct subregions within a single tissue and facilitating mechanistic exploration of the pathogenesis underlying metabolic diseases. Emerging single-cell and spatial metabolomics technologies, as exemplified by recent applications in cancer metabolism, offer new avenues to address these challenges [25,34].

In summary, this unified in vivo flux quantification toolkit addresses critical gaps in existing stable-isotope tracing methodologies, enabling parallel absolute flux analysis in liver and skeletal muscle. The discovery of activity-flux dissociation during fasting exemplifies the unique insights accessible via absolute flux measurement that are obscured by conventional relative quantification strategies. Moving forward, this platform provides a broadly applicable experimental blueprint to map inter-organ carbon communication, define mechanisms of diet-induced metabolic dysfunction, and quantitatively evaluate metabolism-targeted therapeutic candidates.

Figure legends

Figure 1. Schematic overview and validation of the in vivo [$^{13}C_6$]glucose tracing platform for hepatic carbon flux analysis under ad libitum and fasting conditions
(a) Workflow of the 120-min primed-continuous [$^{13}C_6$]glucose infusion strategy applied in awake mice. (b) Schematic illustrating major isotopologue generation patterns of central glycolytic and TCA cycle metabolites derived from fully labeled glucose. (c) Steady-state blood tracer enrichment achieved at the endpoint of infusion, confirming minimal perturbation of endogenous physiological metabolism. (d–f) Simplified metabolic network models for quantitative resolution of hepatic glycolysis, gluconeogenesis, lipogenesis,

TCA cycling, and anaplerotic/cataplerotic fluxes used for flux calculation. $V_{futile\ cycle}$, glucose futile cycle flux; V_{GNG}, glucogenic amino acids, lactate flux; $V_{glycogenesis}$, hepatic glycogen synthesis flux; $V_{glycogenolysis,}$ hepatic glycogenolysis flux; $V_{glycerol}$, flux of glycerol involved in gluconeogenesis; V_{β}, fatty acid β-oxidation flux; $V_{FA\ uptake}$, hepatic fatty acid uptake flux; V_{PC}, flux of glucose generated via pyruvate carboxylase (PC); $V_{PC(T)}$, flux of glucose generated via PC and traversing the TCA cycle; V_{ME}, flux of glucose generated via malic enzyme (ME); $V_{ME(T)}$, flux of glucose generated via ME and traversing the TCA cycle; $V_{PDH(T)}$, flux of glucose generated via pyruvate dehydrogenase (PDH) and traversing the TCA cycle; $V_{PC(DNL)}$, flux of *de novo lipogenesis* (DNL) generated via PC; $V_{ME(DNL)}$, flux of DNL generated via ME; $V_{PDH(DNL)}$, flux of DNL generated via PDH; V_{IDH}, flux through isocitrate dehydrogenase (IDH); V_{GLS}, flux through glutaminase (GLS); $V_{MUT(net)}$, net flux through methylmalonyl-CoA mutase (MUT); $V_{SCS(net)}$, net flux through succinyl-CoA synthetase (SCS); V_{OGDH}, flux through oxoglutarate dehydrogenase (OGDH); $V_{FH(F)}$, flux through fumarase (FH) in the forward direction; $V_{FH(R)}$, flux through FH in the reverse direction. Data are presented as mean ± SEM.

Figure 2. Fasting rewires isotopic labeling profiles and suppresses core hepatic carbon fluxes in chow-fed and high-fat-fed mice

(a–g) Normalized relative isotopic enrichment of pyruvate and major TCA cycle intermediates (citrate, glutamate, glutamine, succinate, fumarate, malate) at distinct m+1, m+2, and m+3 isotopologue positions in ad libitum-fed (RC) and overnight-fasted (RF) chow mice. (h–l) Quantified hepatic carbon fluxes in RC versus RF mice, including whole-body glucose turnover, futile cycling, glycogenolysis, glycerol-derived gluconeogenesis, lipogenic precursor fluxes, fatty acid β-oxidation, net gluconeogenesis, and comprehensive TCA cycle/anaplerotic fluxes. (m–s) Normalized isotopic labeling patterns of hepatic glycolytic and TCA metabolites in ad libitum HFD-fed (HFD) and overnight-fasted HFD (HF) mice. (t–x) Systematic quantification of hepatic glucose turnover, substrate cycling, lipogenic precursor supply, β-oxidation, net gluconeogenic flux, and mitochondrial TCA/anaplerotic fluxes in HFD versus HF mice. All data demonstrate that fasting broadly restrains hepatic glucose-derived carbon incorporation, suppresses glycolytic, lipogenic, and oxidative fluxes, and switches net hepatic glucose balance toward gluconeogenesis under both chow and high-fat dietary conditions. Data are

presented as mean ± SEM. Statistical significance was determined via two-way ANOVA for multiple-group comparisons, and unpaired Student's t-test for pairwise comparisons between two groups: *$p < 0.05$, **$p < 0.01$, ***$p < 0.001$, ****$p < 0.0001$.

Figure 3. Fasting inhibits glucose carbon influx and remodels flux distribution in skeletal muscle

(a–g) Normalized relative ^{13}C enrichment of pyruvate and TCA cycle intermediates in skeletal muscle under fed and fasting states. (h) Quantitative flux profiling reveals suppressed skeletal muscle glucose uptake, glycogenolysis, and pyruvate-driven anaplerotic and TCA entry fluxes upon fasting, whereas total TCA turnover and fatty acid β-oxidation remain stable. (i–o) Normalized isotopic labeling signatures of skeletal muscle metabolites in HFD-fed and fasted HFD mice. (p) Summary of fasting-induced skeletal muscle flux alterations in obese mice, showing restricted glucose carbon utilization and selective suppression of glycolysis-linked mitochondrial fluxes without perturbation of overall TCA cycling and lipid oxidation capacity. Data are presented as mean ± SEM. Statistical significance was determined via two-way ANOVA for multiple-group comparisons, and unpaired Student's t-test for pairwise comparisons between two groups: *$p < 0.05$, **$p < 0.01$, ***$p < 0.001$, ****$p < 0.0001$.

Figure 4. Aldometanib induces extensive hepatic metabolic reprogramming and restricts skeletal muscle glucose carbon flux in HFD mice

(a–g) Normalized isotopic enrichment of hepatic glycolytic and TCA cycle intermediates in vehicle- and Aldometanib-treated HFD mice. (h–l) Quantitative hepatic flux analysis showing elevated whole-body glucose turnover, enhanced substrate cycling, glycerol gluconeogenesis, lipogenic precursor fluxes, and β-oxidation, alongside reduced net gluconeogenic flux and selective remodeling of TCA/anaplerotic fluxes upon Aldometanib administration. (m–s) Normalized skeletal muscle isotopic labeling profiles, showing unaltered metabolite isotopologue patterns after Aldometanib treatment. (t) Skeletal muscle carbon flux quantification demonstrating that Aldometanib significantly suppresses glucose uptake, glycogenolysis, and pyruvate-dependent TCA entry fluxes, thereby restricting glucose carbon influx into muscle mitochondrial metabolism without altering basal TCA cycling or β-oxidation capacity. Data are presented as mean ± SEM. Statistical significance was determined via two-way ANOVA for multiple-group

comparisons, and unpaired Student's t-test for pairwise comparisons between two groups: *$p < 0.05$, **$p < 0.01$, ***$p < 0.001$, ****$p < 0.0001$.

Figure 5. Metformin drives distinct hepatic flux remodeling and enhances skeletal muscle anaplerotic and oxidative metabolism in HFD mice

(a–g) Normalized hepatic isotopic enrichment of glycolytic and TCA metabolites in vehicle- and metformin-treated obese mice, showing altered pyruvate isotopic distribution and elevated fumarate labeling. (h–l) Hepatic flux quantification revealing increased glucose turnover and combined pyruvate carboxylase/malic enzyme anaplerosis, elevated lipogenic pyruvate dehydrogenase flux, and reduced hepatic anaplerotic cycling upon metformin treatment, with unaltered net gluconeogenesis. (m–s) Normalized skeletal muscle isotopic enrichment patterns. (t) Skeletal muscle flux profiles demonstrating that metformin markedly enhances muscle anaplerotic flux, total TCA turnover, β-oxidation, and net glutaminolysis, indicating divergent tissue-specific metabolic regulation compared with Aldometanib. Data are presented as mean ± SEM. Statistical significance was determined via two-way ANOVA for multiple-group comparisons, and unpaired Student's t-test for pairwise comparisons between two groups: *$p < 0.05$, **$p < 0.01$, ***$p < 0.001$, ****$p < 0.0001$.

Supplemental Figure 1. Raw isotopic labeling and multi-tracer validation of fasting-induced hepatic metabolic remodeling

(a–g) Raw unnormalized ^{13}C isotopic enrichment of hepatic metabolites in chow-fed control and fasted mice. (h–n) Raw hepatic isotopic labeling profiles in ad libitum and fasted HFD mice. (o–q) Independent validation using [$^{13}C_3$]alanine and 1,2,3,4,5,6-^{13}C-palmitate tracers, confirming enhanced amino acid-dependent gluconeogenic activity and elevated fatty acid β-oxidation pathway activity despite reduced absolute β-oxidation flux during fasting. Data are presented as mean ± SEM. Statistical significance was determined via two-way ANOVA for multiple-group comparisons, and unpaired Student's t-test for pairwise comparisons between two groups: *$p < 0.05$, **$p < 0.01$, ***$p < 0.001$, ****$p < 0.0001$.

Supplemental Figure 2. Basal skeletal muscle isotopic signatures under fed and fasting conditions

(a) Schematic of skeletal muscle tracing analysis. (b–h) Raw skeletal muscle metabolite

isotopic enrichment in chow-fed and fasted mice. (i–o) Raw isotopic labeling profiles in HFD-fed and fasted obese mice, illustrating modest baseline isotopic alterations prior to normalization and flux quantification. Data are presented as mean ± SEM. Statistical significance was determined via two-way ANOVA for multiple-group comparisons, and unpaired Student's t-test for pairwise comparisons between two groups: *$p < 0.05$, **$p < 0.01$, ***$p < 0.001$.

Supplemental Figure 3. Body composition and raw hepatic isotopic profiles upon Aldometanib treatment

(a) Relative fat mass and lean mass fraction in vehicle- and Aldometanib-treated HFD mice. (b–h) Raw unnormalized hepatic isotopic enrichment of glycolytic and TCA cycle intermediates following Aldometanib intervention. (i–n) Raw skeletal muscle metabolite isotopic labeling patterns, confirming largely unaltered muscle isotopic signatures after Aldometanib treatment. Data are presented as mean ± SEM. Statistical significance was determined via two-way ANOVA for multiple-group comparisons, and unpaired Student's t-test for pairwise comparisons between two groups: *$p < 0.05$, **$p < 0.01$, ***$p < 0.001$.

Supplemental Figure 4. Raw hepatic and skeletal muscle isotopic enrichment in metformin-treated HFD mice

(a–h) Raw hepatic isotopic enrichment of pyruvate and TCA cycle intermediates in vehicle- versus metformin-administered obese mice. (i–o) Raw skeletal muscle metabolite isotopic labeling profiles, showing selective elevation of malate m+1 enrichment upon metformin treatment. Data are presented as mean ± SEM. Statistical significance was determined via two-way ANOVA for multiple-group comparisons, and unpaired Student's t-test for pairwise comparisons between two groups: *$p < 0.05$, **$p < 0.01$, ***$p < 0.001$, ****$p < 0.0001$.

Acknowledgments

The authors thank all members of our laboratory for their help. This work was supported by the National Natural Science Foundation of China (32571363), Major Innovation Projects of Henan Province (241112310700), Henan Provincial Science and Technology Research Project (252102311146), and China Postdoctoral Science Foundation (2025M771998).

Author contributions

X.Z., Z.D., and Y.W. designed and wrote the manuscript. W.L., G.W., D.G., W.W., M.G., and X.S., performed the experiments. Y.W., W.L. and G.W. analyzed the data and revised the manuscript. All of the authors read and approved the final version of the manuscript for publication.

Declaration of interests

The authors have no competing financial interests to declare.

References

1 Sakuma, I. *et al.* Liver lipid droplet cholesterol content is a key determinant of metabolic dysfunction-associated steatohepatitis. *Proc Natl Acad Sci U S A* **122**, e2502978122, doi:10.1073/pnas.2502978122 (2025).

2 Hu, Y. *et al.* High-fat diet ablates an insulin-responsive pool of GLUT4 glucose transporters in skeletal muscle. *bioRxiv*, doi:10.1101/2025.06.29.662135 (2025).

3 Tanaka, T. *et al.* Hepatic ferredoxin reductase modulates mitochondrial function and iron homeostasis in metabolic dysfunction-associated steatotic liver disease. *Res Sq*, doi:10.21203/rs.3.rs-7014857/v1 (2025).

4 Weilandt, D. R. *et al.* Competitive catabolism drives hyperglycemia and hyperinsulinemia in obesity. *Cell Metabolism*, doi:10.1016/j.cmet.2026.07.001.

5 Novoa, E. *et al.* Lack of PCK1 in hepatic stellate cells causes liver fibrosis by fueling tricarboxylic acid cycle and increasing glycolysis. *Cell Metabolism* **38**, 729-745.e729, doi:10.1016/j.cmet.2026.01.016 (2026).

6 Wessendorf-Rodriguez, K. *et al.* Modeling lipid homeostasis using stable isotope tracing and flux analysis. *Cell Metabolism* **38**, 460-473.e466, doi:10.1016/j.cmet.2026.01.020 (2026).

7 Hubbard, B. T. *et al.* Q-Flux: A method to assess hepatic mitochondrial succinate dehydrogenase, methylmalonyl-CoA mutase, and glutaminase fluxes in vivo. *Cell Metab* **35**, 212-226.e214, doi:10.1016/j.cmet.2022.11.011 (2023).

8 Weilandt, D. R. *et al.* Competitive catabolism drives hyperglycemia and hyperinsulinemia in obesity. *Cell Metabolism*, doi:https://doi.org/10.1016/j.cmet.2026.07.001 (2026).

9 Plant, K. *et al.* Influence of a 12 week at-home resistance exercise program on 13C-glucose metabolism in patients with metabolic myopathies. *Molecular Genetics and Metabolism* **147**, 109714, doi:https://doi.org/10.1016/j.ymgme.2025.109714 (2026).

10 Argilés, J. M., Campos, N., Lopez-Pedrosa, J. M., Rueda, R. & Rodriguez-Mañas, L. Skeletal Muscle Regulates Metabolism via Interorgan Crosstalk: Roles in Health and Disease. *J Am Med Dir Assoc* **17**, 789-796, doi:10.1016/j.jamda.2016.04.019 (2016).

11 Cree-Green, M. *et al.* Nonalcoholic fatty liver disease in obese adolescent females is associated with multi-tissue insulin resistance and visceral adiposity markers. *Metabolism Open* **2**, 100011, doi:https://doi.org/10.1016/j.metop.2019.100011 (2019).

12 Perry, R. J. *et al.* Non-invasive assessment of hepatic mitochondrial metabolism by positional isotopomer NMR tracer analysis (PINTA). *Nat Commun* **8**, 798, doi:10.1038/s41467-017-01143-w (2017).

13 Hubbard, B. T. *et al.* Q-Flux: A method to assess hepatic mitochondrial succinate dehydrogenase, methylmalonyl-CoA mutase, and glutaminase fluxes in vivo. *Cell Metabolism* **35**, 212-226.e214, doi:https://doi.org/10.1016/j.cmet.2022.11.011 (2023).

14 Wang, Y. *et al.* Uncoupling Hepatic Oxidative Phosphorylation Reduces Tumor Growth in Two Murine Models of Colon Cancer. *Cell Rep* **24**, 47-55, doi:10.1016/j.celrep.2018.06.008 (2018).

15 Li, M. *et al.* AMPK targets PDZD8 to trigger carbon source shift from glucose to glutamine. *Cell Res* **34**, 683-706, doi:10.1038/s41422-024-00985-6 (2024).

16 Wang, Y. *et al.* AdipoRon exerts opposing effects on insulin sensitivity via fibroblast growth factor 21-mediated time-dependent mechanisms. *The Journal of biological chemistry* **298**, 101641, doi:10.1016/j.jbc.2022.101641 (2022).

17 Camporez, J. P. *et al.* Mechanism by which arylamine N-acetyltransferase 1 ablation causes insulin resistance in mice. *Proc Natl Acad Sci U S A* **114**, E11285-E11292, doi:10.1073/pnas.1716990115 (2017).

18 Xiang, Y. *et al.* Protocatechuic Acid Ameliorates High Fat Diet-Induced Obesity and Insulin Resistance in Mice. *Mol Nutr Food Res* **67**, e2200244, doi:10.1002/mnfr.202200244 (2023).

19 Hundal, R. S. *et al.* Mechanism by which metformin reduces glucose production in type 2 diabetes. *Diabetes* **49**, 2063-2069, doi:10.2337/diabetes.49.12.2063 (2000).

20 Hasenour, C. M. *et al.* Mass spectrometry-based microassay of (2)H and (13)C plasma glucose labeling to quantify liver metabolic fluxes in vivo. *Am J Physiol Endocrinol Metab* **309**, E191-203, doi:10.1152/ajpendo.00003.2015 (2015).

21 Sellers, K. *et al.* Pyruvate carboxylase is critical for non-small-cell lung cancer proliferation. *J Clin Invest* **125**, 687-698, doi:10.1172/jci72873 (2015).

22 Orman, M. A., Androulakis, I. P., Berthiaume, F. & Ierapetritou, M. G. Metabolic network analysis of perfused livers under fed and fasted states: incorporating thermodynamic and futile-cycle-associated regulatory constraints. *J Theor Biol* **293**, 101-110, doi:10.1016/j.jtbi.2011.10.019 (2012).

23 Hubbard, B. T. *et al.* Insulin receptor(T1160) phosphorylation mediates renal cortical insulin resistance but not excess gluconeogenesis from glycerol. *Nat Commun* **17**, doi:10.1038/s41467-026-73016-0 (2026).

24 Moon, S. J. *et al.* Modeling tissue-specific Drosophila metabolism identifies high sugar diet-induced metabolic dysregulation in muscle at reaction and pathway levels. *Nat Commun* **17**, 1692, doi:10.1038/s41467-026-68395-3 (2026).

25 Meghdadi, B. *et al.* Digital twins for in vivo metabolic flux estimations in patients with brain cancer. *Cell Metab* **38**, 228-246.e217, doi:10.1016/j.cmet.2025.10.022 (2026).

26 Satapati, S. *et al.* Mitochondrial metabolism mediates oxidative stress and inflammation in fatty liver. *J Clin Invest* **126**, 1605, doi:10.1172/jci86695 (2016).

27 Chouchani, E. T. *et al.* Ischaemic accumulation of succinate controls reperfusion injury through mitochondrial ROS. *Nature* **515**, 431-435, doi:10.1038/nature13909 (2014).

28 Wessendorf-Rodriguez, K. *et al.* Modeling lipid homeostasis using stable isotope tracing and flux analysis. *Cell Metab* **38**, 460-473.e466, doi:10.1016/j.cmet.2026.01.020 (2026).

29 Sebo, Z. L. *et al.* Metformin inhibits mitochondrial complex I in intestinal epithelium to promote glycaemic control. *Nat Metab* **8**, 1291-1304, doi:10.1038/s42255-026-01530-y (2026).

30 Gormsen, L. C. *et al.* Metformin increases endogenous glucose production in non-diabetic individuals and individuals with recent-onset type 2 diabetes. *Diabetologia* **62**, 1251-1256, doi:10.1007/s00125-019-4872-7 (2019).

31 Ma, T. *et al.* Low-dose metformin targets the lysosomal AMPK pathway through PEN2. *Nature* **603**, 159-165, doi:10.1038/s41586-022-04431-8 (2022).

32 Zhang, C. S. *et al.* Metformin Activates AMPK through the Lysosomal Pathway. *Cell Metab* **24**, 521-522, doi:10.1016/j.cmet.2016.09.003 (2016).

33 Perry, R. J. *et al.* Leptin Mediates a Glucose-Fatty Acid Cycle to Maintain Glucose Homeostasis in Starvation. *Cell* **172**, 234-248.e217, doi:10.1016/j.cell.2017.12.001 (2018).

34 Paloviita, P. *et al.* Integrated transcriptomic analysis reveals metabolic remodeling and gene expression networks related to human 8-cell-stage embryo-like cells. *Cell Rep* **45**, 116748, doi:10.1016/j.celrep.2025.116748 (2026).

Figures

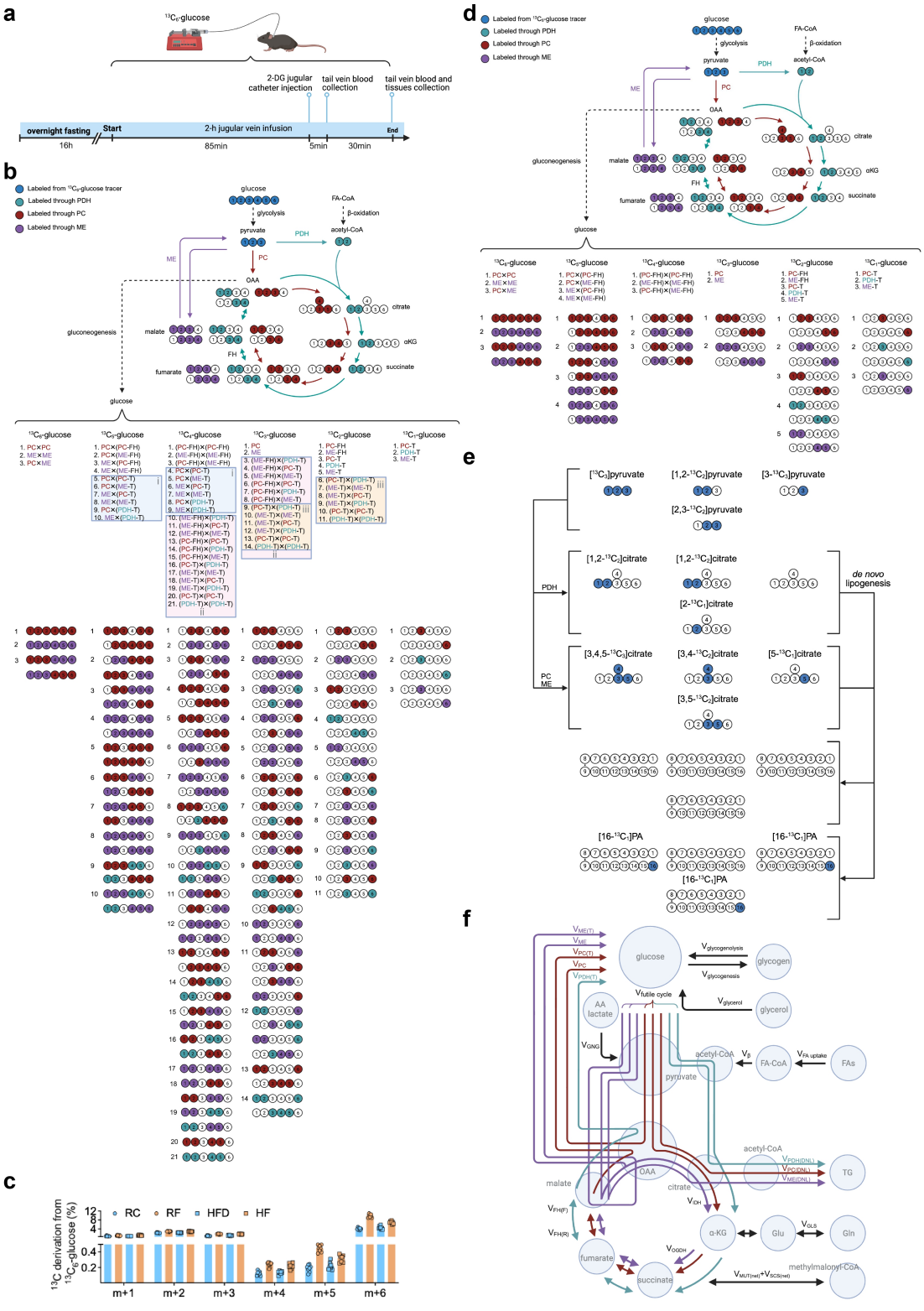


Figure 1

Schematic overview and validation of the in vivo [$^{13}C_6$]glucose tracing platform for hepatic carbon flux analysis under ad libitum and fasting conditions

(a) Workflow of the 120-min primed-continuous [$^{13}C_6$]glucose infusion strategy applied in awake mice. (b) Schematic illustrating major isotopologue generation patterns of central glycolytic and TCA cycle metabolites derived from fully labeled glucose. (c) Steady-state blood tracer enrichment achieved at the endpoint of infusion, confirming minimal perturbation of endogenous physiological metabolism. (d–f) Simplified metabolic network models for quantitative resolution of hepatic glycolysis, gluconeogenesis, lipogenesis, TCA cycling, and anaplerotic/cataplerotic fluxes used for flux calculation. $V_{futile\ cycle}$, glucose futile cycle flux; V_{GNG}, glucogenic amino acids, lactate flux; $V_{glycogenesis}$, hepatic glycogen synthesis flux; $V_{glycogenolysis,}$ hepatic glycogenolysis flux; $V_{glycerol}$, flux of glycerol involved in gluconeogenesis; V_{β}, fatty acid β-oxidation flux; $V_{FA\ uptake}$, hepatic fatty acid uptake flux; V_{PC}, flux of glucose generated via pyruvate carboxylase (PC); $V_{PC(T)}$, flux of glucose generated via PC and traversing the TCA cycle; V_{ME}, flux of glucose generated via malic enzyme (ME); $V_{ME(T)}$, flux of glucose generated via ME and traversing the TCA cycle; $V_{PDH(T)}$, flux of glucose generated via pyruvate dehydrogenase (PDH) and traversing the TCA cycle; $V_{PC(DNL)}$, flux of *de novo lipogenesis* (DNL) generated via PC; $V_{ME(DNL)}$, flux of DNL generated via ME; $V_{PDH(DNL)}$, flux of DNL generated via PDH; V_{IDH}, flux through isocitrate dehydrogenase (IDH); V_{GLS}, flux through glutaminase (GLS); $V_{MUT(net)}$, net flux through methylmalonyl-CoA mutase (MUT); $V_{SCS(net)}$, net flux through succinyl-CoA synthetase (SCS); V_{OGDH}, flux through oxoglutarate dehydrogenase (OGDH); $V_{FH(F)}$, flux through fumarase (FH) in the forward direction; $V_{FH(R)}$, flux through FH in the reverse direction. Data are presented as mean ± SEM.

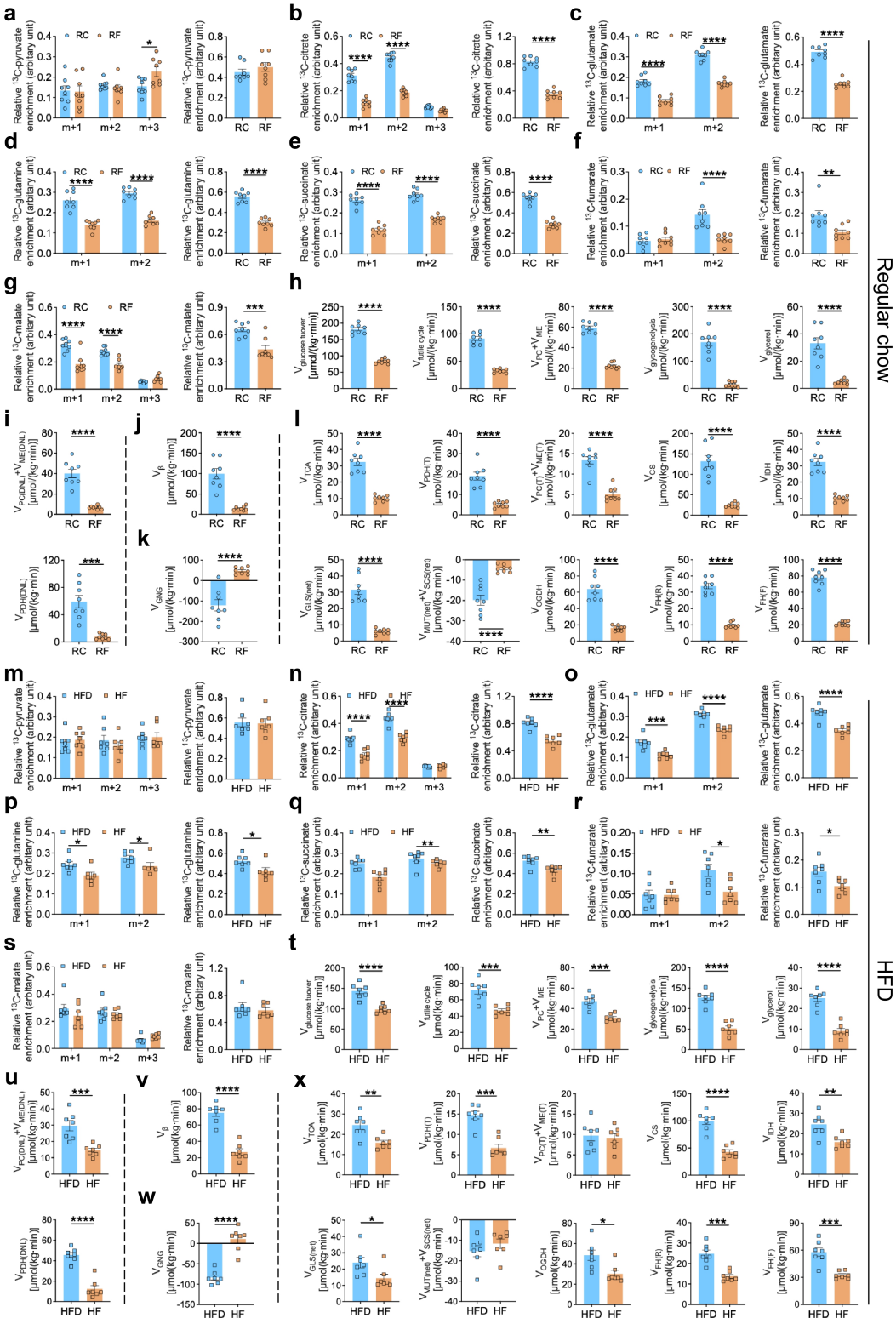


Figure 2

Fasting rewires isotopic labeling profiles and suppresses core hepatic carbon fluxes in chow-fed and high-fat-fed mice

(a–g) Normalized relative isotopic enrichment of pyruvate and major TCA cycle intermediates (citrate, glutamate, glutamine, succinate, fumarate, malate) at distinct m+1, m+2, and m+3 isotopologue

positions in ad libitum-fed (RC) and overnight-fasted (RF) chow mice. (h–l) Quantified hepatic carbon fluxes in RC versus RF mice, including whole-body glucose turnover, futile cycling, glycogenolysis, glycerol-derived gluconeogenesis, lipogenic precursor fluxes, fatty acid β-oxidation, net gluconeogenesis, and comprehensive TCA cycle/anaplerotic fluxes. (m–s) Normalized isotopic labeling patterns of hepatic glycolytic and TCA metabolites in ad libitum HFD-fed (HFD) and overnight-fasted HFD (HF) mice. (t–x) Systematic quantification of hepatic glucose turnover, substrate cycling, lipogenic precursor supply, β-oxidation, net gluconeogenic flux, and mitochondrial TCA/anaplerotic fluxes in HFD versus HF mice. All data demonstrate that fasting broadly restrains hepatic glucose-derived carbon incorporation, suppresses glycolytic, lipogenic, and oxidative fluxes, and switches net hepatic glucose balance toward gluconeogenesis under both chow and high-fat dietary conditions. Data are presented as mean ± SEM. Statistical significance was determined via two-way ANOVA for multiple-group comparisons, and unpaired Student's t-test for pairwise comparisons between two groups: *p< 0.05, **p < 0.01, ***p < 0.001, ****p < 0.0001.

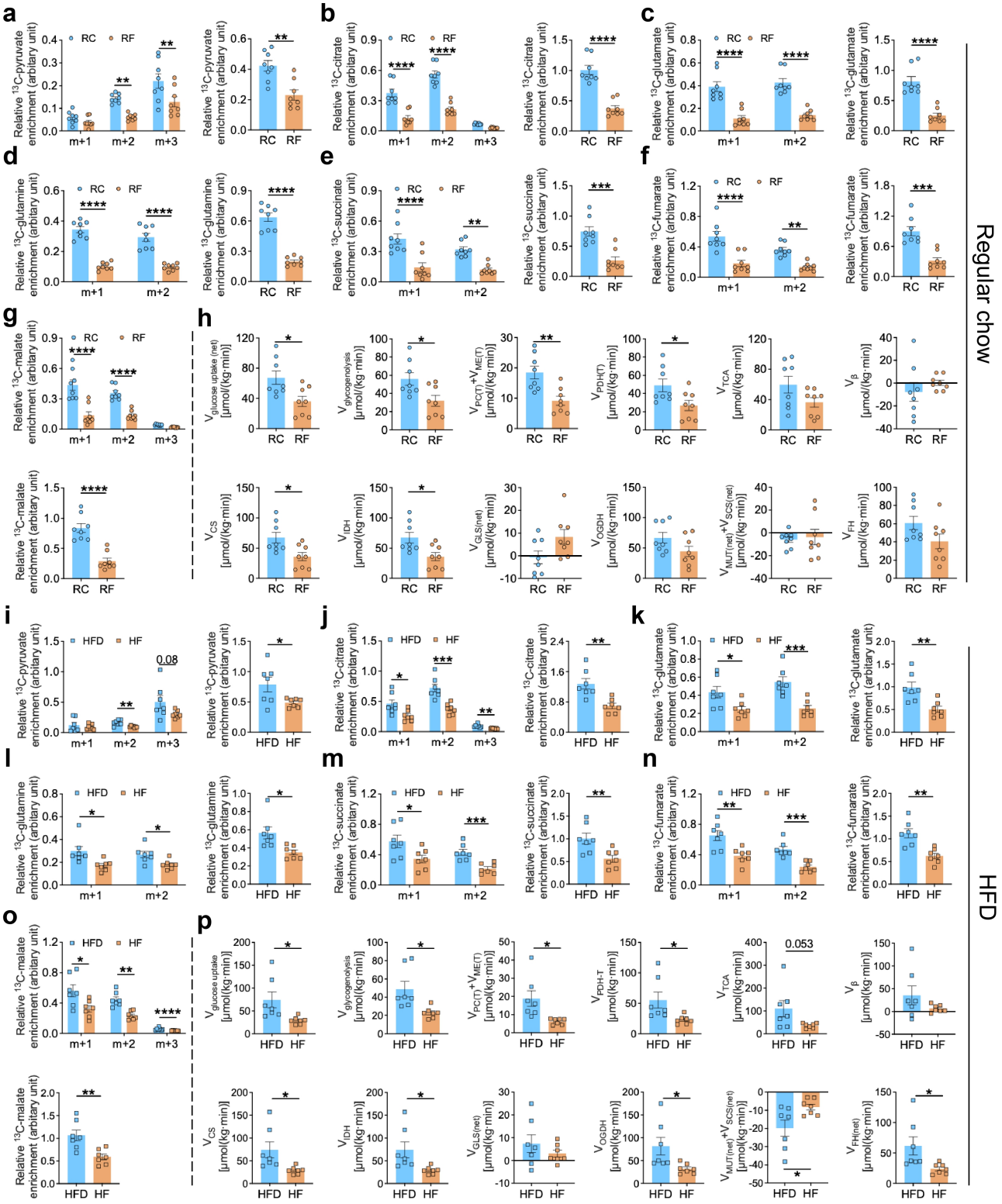


Figure 3

Fasting inhibits glucose carbon influx and remodels flux distribution in skeletal muscle

(a–g) Normalized relative ^{13}C enrichment of pyruvate and TCA cycle intermediates in skeletal muscle under fed and fasting states. (h) Quantitative flux profiling reveals suppressed skeletal muscle glucose uptake, glycogenolysis, and pyruvate-driven anaplerotic and TCA entry fluxes upon fasting, whereas total

TCA turnover and fatty acid β-oxidation remain stable. (i–o) Normalized isotopic labeling signatures of skeletal muscle metabolites in HFD-fed and fasted HFD mice. (p) Summary of fasting-induced skeletal muscle flux alterations in obese mice, showing restricted glucose carbon utilization and selective suppression of glycolysis-linked mitochondrial fluxes without perturbation of overall TCA cycling and lipid oxidation capacity. Data are presented as mean ± SEM. Statistical significance was determined via two-way ANOVA for multiple-group comparisons, and unpaired Student's t-test for pairwise comparisons between two groups: *$p < 0.05$, **$p < 0.01$, ***$p < 0.001$, ****$p < 0.0001$.

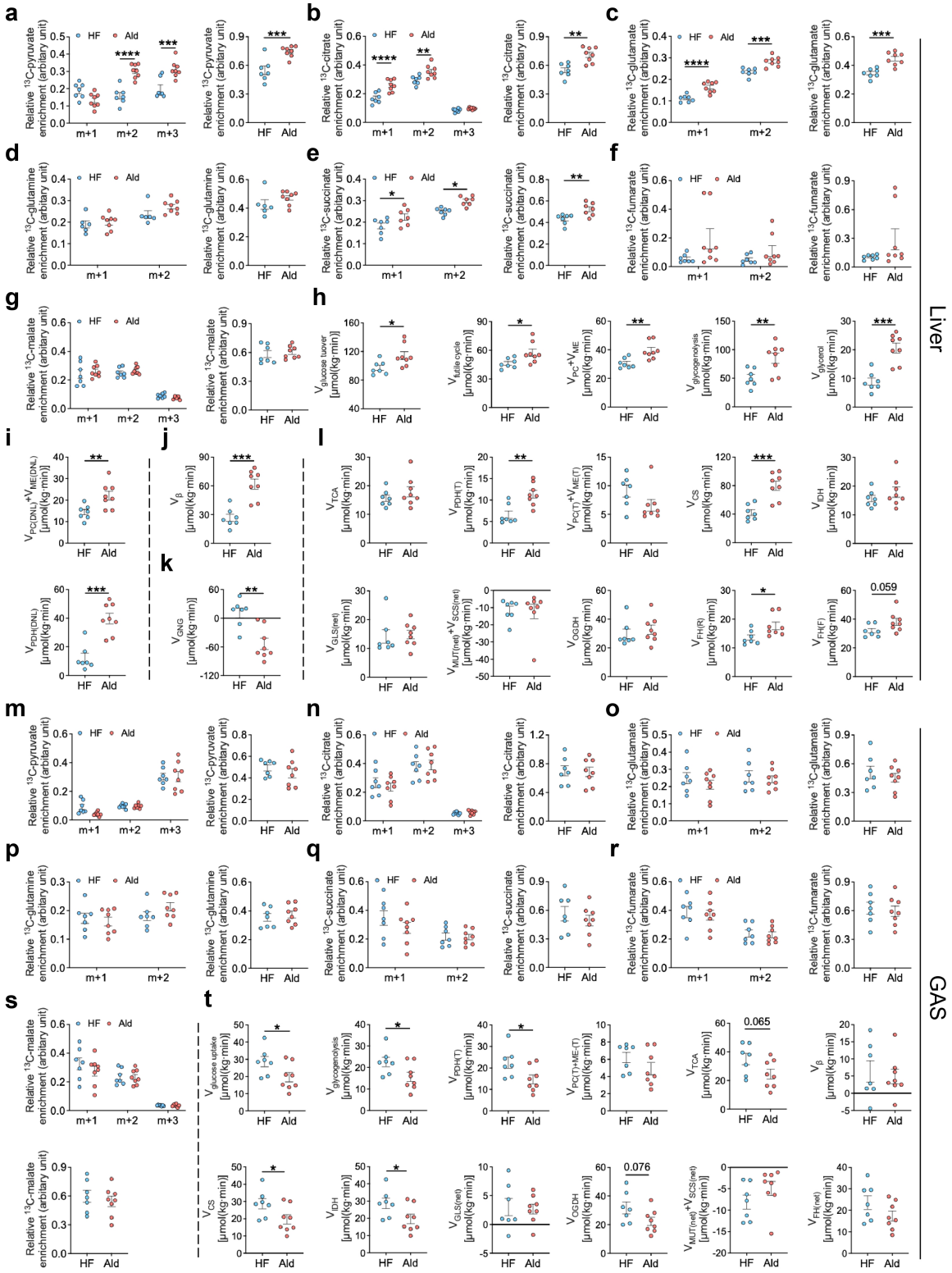


Figure 4

Aldometanib induces extensive hepatic metabolic reprogramming and restricts skeletal muscle glucose carbon flux in HFD mice

(a–g) Normalized isotopic enrichment of hepatic glycolytic and TCA cycle intermediates in vehicle- and Aldometanib-treated HFD mice. (h–l) Quantitative hepatic flux analysis showing elevated whole-body glucose turnover, enhanced substrate cycling, glycerol gluconeogenesis, lipogenic precursor fluxes, and β-oxidation, alongside reduced net gluconeogenic flux and selective remodeling of TCA/anaplerotic fluxes upon Aldometanib administration. (m–s) Normalized skeletal muscle isotopic labeling profiles, showing unaltered metabolite isotopologue patterns after Aldometanib treatment. (t) Skeletal muscle carbon flux quantification demonstrating that Aldometanib significantly suppresses glucose uptake, glycogenolysis, and pyruvate-dependent TCA entry fluxes, thereby restricting glucose carbon influx into muscle mitochondrial metabolism without altering basal TCA cycling or β-oxidation capacity. Data are presented as mean ± SEM. Statistical significance was determined via two-way ANOVA for multiple-group comparisons, and unpaired Student's t-test for pairwise comparisons between two groups: *p < 0.05, **p < 0.01, ***p< 0.001, ****p < 0.0001.

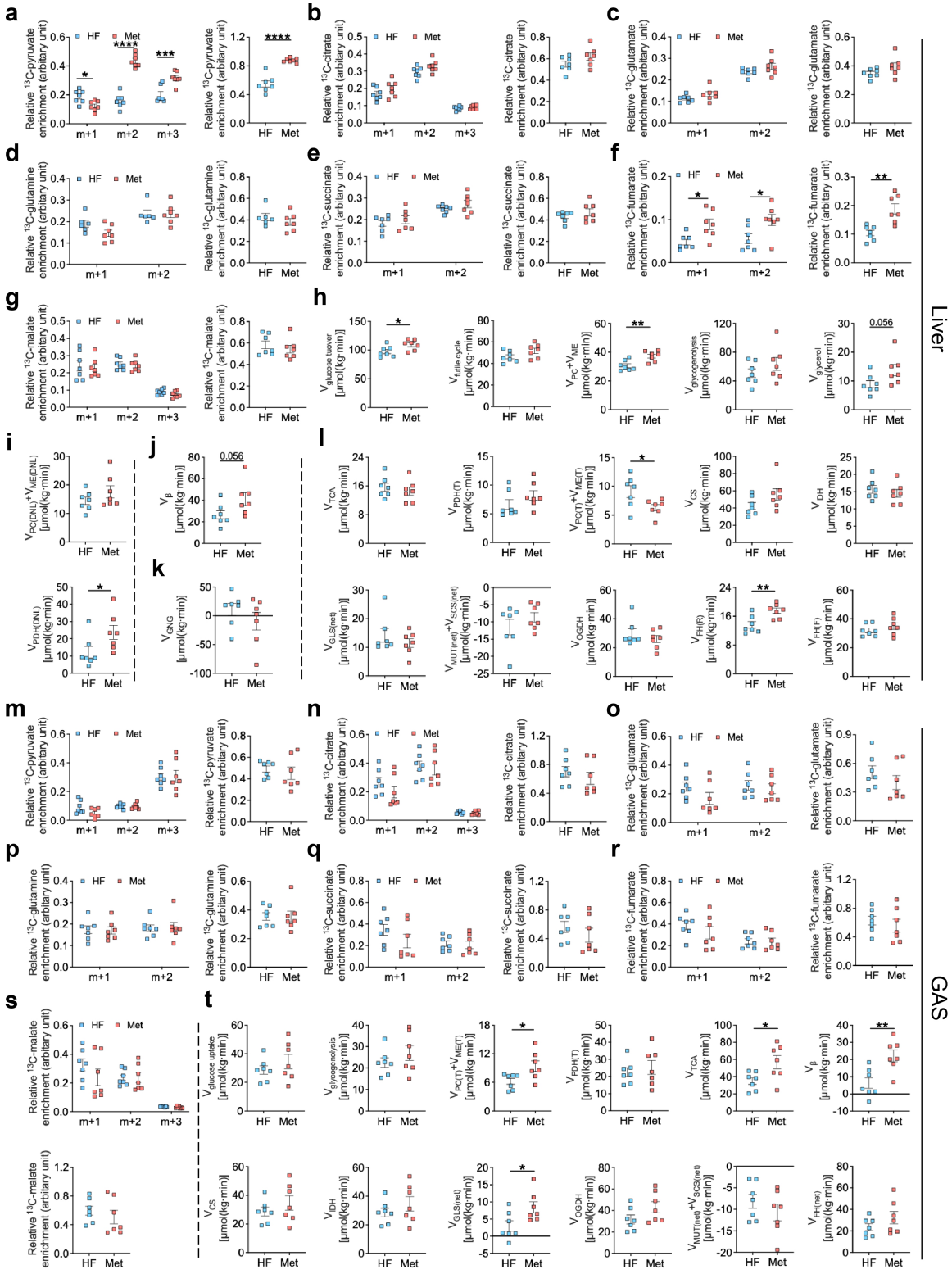


Figure 5

Metformin drives distinct hepatic flux remodeling and enhances skeletal muscle anaplerotic and oxidative metabolism in HFD mice

(a–g) Normalized hepatic isotopic enrichment of glycolytic and TCA metabolites in vehicle- and metformin-treated obese mice, showing altered pyruvate isotopic distribution and elevated fumarate

labeling. (h–l) Hepatic flux quantification revealing increased glucose turnover and combined pyruvate carboxylase/malic enzyme anaplerosis, elevated lipogenic pyruvate dehydrogenase flux, and reduced hepatic anaplerotic cycling upon metformin treatment, with unaltered net gluconeogenesis. (m–s) Normalized skeletal muscle isotopic enrichment patterns. (t) Skeletal muscle flux profiles demonstrating that metformin markedly enhances muscle anaplerotic flux, total TCA turnover, β-oxidation, and net glutaminolysis, indicating divergent tissue-specific metabolic regulation compared with Aldometanib. Data are presented as mean ± SEM. Statistical significance was determined via two-way ANOVA for multiple-group comparisons, and unpaired Student's t-test for pairwise comparisons between two groups: *p< 0.05, **p < 0.01, ***p < 0.001, ****p < 0.0001.

Supplementary Files

This is a list of supplementary files associated with this preprint. Click to download.

- FigureS4.jpg
- FigureS3.jpg
- FigureS1.jpg
- FigureS2.jpg